Joint Design of Communication Sensing and Control With a UAV Platform

Qingliang Li, *Graduate Student Member, IEEE*, Bin Li, *Senior Member, IEEE*, Zhen-Qing He, *Member, IEEE*, Yue Rong, *Senior Member, IEEE*, and Zhu Han, *Fellow, IEEE*

***Abstract*— In this article, a joint design of communication sensing and control (JDCSC) scheme is developed which focuses on a scenario where a cellular-connected unmanned aerial vehicles (UAV) senses a moving target. The goal is to maximize the sensing mutual information via jointly optimizing the transmit power, the trajectory of the UAV and the task completion time, while meeting the onboard energy, the communication service quality, and the UAV flight safety constraints. In particular, UAV dynamics are considered, which are usually ignored in the existing design and inferior communication and sensing quality of service might be resulted. The formulated problem is dynamic optimization problem, which is difficult to be solved. The control parameterization method and exact penalty function scheme are utilized to transform the problem into a static nonlinear program which can be solved by gradient-based methods. The effectiveness of the JDCSC approach is verified by carrying out some numerical examples.**

***Index Terms*— Joint design sensing communication and control, 6G, quadrotor UAV, trajectory optimization, exact penalty function.**

I. Introduction

INTEGRATED sensing and communication (ISAC) along with ubiquitous communication have been identified by the International Telecommunication Union (ITU) as pivotal application scenarios for 6G, fostering numerous disruptive innovations in applications [1]. The existing ISAC methods can be generally classified into three categories: radar-communication (RadCom) [2], dual-functional radar communication (DFRC) [3], [4], and joint communication and radar sensing (JCAS) [5], [6]. RadCom schemes try to embed communication information in radar waveforms for communication. However, they only support very low communication rates. Communication-driven DFRC schemes attempt to identify target data from signals, such as using specific frames for perception through time-division techniques. JCAS tries to propose novel waveforms with dual-function of communication sensing to enable simultaneous high-rate communications and high-accuracy sensing [5], [7].

Unmanned aerial vehicles (UAVs) connected to cellular networks are regarded as a pivotal approach for achieving beyond visual line-of-sight (BVLoS) control and ubiquitous coverage of drones [8], [9], [10], [11]. In contrast to the device-to-device (D2D) links that typically operate in unlicensed spectrums, cellular-connected UAVs work within licensed spectrums, offering more flexible and universally accessible network services to both base stations (BSs) and ground users [8], [9]. Leveraging the altitude advantages of UAVs and the superior performance of cellular networks, cellular-connected UAVs can establish robust line-of-sight (LoS) links, providing wireless communication services with higher capacity, greater reliability, and lower latency [10]. Furthermore, the 3rd Generation Partnership Project (3GPP) is actively advancing the standardization process for the integration of UAVs into cellular networks [11].

When cellular-connected UAV meets ISAC, the following benefits can be obtained [12]. Firstly, originally independent communication and sensing (C&S) loads can be integrated into the ISAC load through resource sharing, thus reducing the load weight and improving the endurance of UAVs. Secondly, compared with separately designed C&S platforms, the ISAC improves both the communication capability and the sensing performance. Thirdly, UAV-enabled ISAC (UAV-ISAC) can provide a broader and more flexible service coverage than terrestrial BS ISAC (BS-ISAC) that can only provide C&S services within a limited range [13]. Moreover, by leveraging the ISAC technology, UAVs are able to enhance their flight safety by acquiring information on cooperative targets through communication signals and actively sensing the position of non-cooperative targets in the environment to avoid collisions.

By optimizing the trajectory of UAV, the flexible maneuverability of UAV can be fully utilized to improve ISAC performance. A time-division multiple access (TDMA) based periodic ISAC mechanism is proposed in [13], where the simulation results demonstrate the significant role of UAV trajectory design in balancing the C&S performance. [14] investigated cellular-connected UAV for conducting sensing

Received 1 March 2024; revised 14 July 2024; accepted 9 October 2024. Date of publication 22 October 2024; date of current version 12 December 2024. This work was supported in part by the National Natural Science Foundation of China under Grant 62071317; in part by the National Defense Basic Scientific Research Program of China under Grant JCKY2021204B051; in part by NSF under Grant CNS-2107216, Grant CNS-2128368, Grant CMMI-2222810, and Grant ECCS-2302469; in part by U.S. Department of Transportation; in part by Toyota; in part by Amazon; and in part by Japan Science and Technology Agency (JST) Adopting Sustainable Partnerships for Innovative Research Ecosystem (ASPIRE) under Grant JPMJAP2326. The associate editor coordinating the review of this article and approving it for publication was S. R. Khosravirad. *(Corresponding author: Bin Li.)*

Qingliang Li, Bin Li, and Zhen-Qing He are with the School of Aeronautics and Astronautics, Sichuan University, Chengdu 610065, China (e-mail: liqingliang@stu.scu.edu.cn; bin.li@scu.edu.cn; zhenqinghe@scu.edu.cn).

Yue Rong is with the School of Electrical Engineering, Computing and Mathematical Sciences, Curtin University, Perth, WA 6845, Australia (e-mail: y.rong@curtin.edu.au).

Zhu Han is with the Department of Electrical and Computer Engineering at the University of Houston, Houston, TX 77004 USA, and also with the Department of Computer Science and Engineering, Kyung Hee University, Seoul 446-701, South Korea (e-mail: zhan2@uh.edu).

Color versions of one or more figures in this article are available at https://doi.org/10.1109/TWC.2024.3480705.

Digital Object Identifier 10.1109/TWC.2024.3480705

tasks and uploading the sensed data in real-time to a BS, with the objective of minimizing the task completion time. To achieve this goal, the UAV's two dimensional (2D) trajectory, the sensing order of each task, and the association between the UAV and the BS are optimized. In [15], static deployment and planar motion scenarios of UAVs are discussed. They propose a joint design for UAV trajectory or static deployment and ISAC beamforming to maximize user throughput while considering constraints such as sensing beam gain, transmission power, and practical flight limitations.

References [13], [14], and [15] focus on optimizing the path of UAV under the constraint of the maximum speed. This approach simplifies the UAV as a mass point and used a discretized trajectory framework that focuses on the UAV's kinematics. However, the UAV is not just a mass point but a rigid-body with both translational and rotational motion [16]. It is a complex dynamical system where motion is influenced by both kinematics and dynamics [17].

Recently, there are some works that plan UAV trajectories by considering the dynamics of UAVs. A control parameterization framework is utilized for UAV-aided communication [17] and for UAV formations [18]. Furthermore, the Gauss pseudo-spectral method (GPM) is applied in [19] and [20] to explore the control of fixed-wing UAV formations and the obstacle avoidance of a quadrotor UAV, respectively. For the significant nonlinearity of the dynamics of quadrotor, [21] and [22] explore methods for transforming non-convex problems into convex sub-problems. Specifically, [21] focuses on achieving iterative optimization of time-optimal trajectories by transforming the non-convex problem into a second-order cone programming (SOCP) sub-problem. In contrast, [22] employs a three dimensional (3D) trajectory as an initial estimate and then derive a 6 degrees of freedom (6DoF) trajectory through iterative solutions via sequential convex programming (SCP). Inspired by artificial intelligence (AI), machine learning techniques are leveraged in [23] and [24] for planning the 6DoF trajectory of a fixed-wing UAV in obstacle avoidance scenarios.

While trajectory planning incorporating UAV dynamics has received significant attention in the fields of obstacle avoidance and formation control, there is a lack of research on UAV-aided communications and sensing. The trajectories generated by the existing design in UAV communication field lack smoothness and usually lead to trajectory distortion. Moreover, the planned path cannot be effectively tracked by the UAV's controller in real world applications. Consequently, this can result in C&S performance degradation, including reduced communication throughput rate, increased packet loss, and distorted data perception, as shown in Fig. 1.

Inspired by the aforementioned discussions, a joint design of communication sensing and control (JDCSC) optimization framework is proposed, which generates a 3D smooth trajectory by accounting for the UAV's rigid-body dynamics. In this framework, we focus on a scenario, as depicted in Fig. 2, where a cellular-connected UAV senses a mobile target (vehicle) with an ISAC system and an optical camera. This considered framework has various potential applications, such as traffic monitoring and live broadcasting of outdoor events.

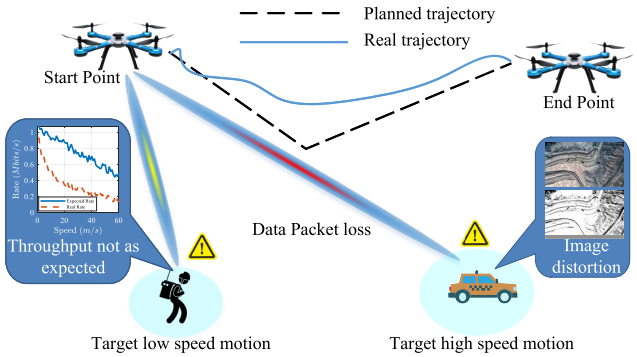

Fig. 1. Paths planned by existing design framework affect communication and sensing QoS in real trajectory.

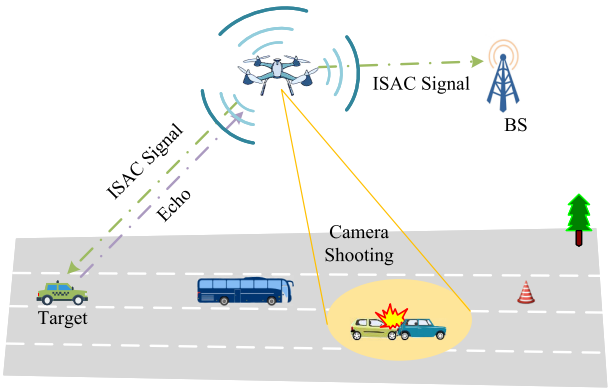

Fig. 2. An illustration of a UAV-ISAC system.

In contrast to traditional methods [13], [14], [15] that focus on stationary targets, this study takes into account the continuous trajectories of both the UAV and the target, thereby improving the general applicability of the problem. Furthermore, instead of discretizing the trajectories of the UAV and the mobile target, a segment-based parameterization method is utilized for the UAV's control signals to guarantee the continuity and smoothness of the UAV's dynamic trajectory. The proposed algorithm effectively addresses the challenges posed by multiple constraints through the application of an exact penalty function, which aids in reducing the algorithm's complexity. The following is a summary of this manuscript's primary contributions.

- We propose a novel framework for trajectory design within UAV-ISAC system, incorporating the dynamics of the UAV as a pivotal element. Comparing with [13], [14], and [15], in which the planned trajectories are piece-wise line constant, a smooth trajectory is obtained by the proposed algorithm.
- The control parameterization method and an exact penalty function scheme are employed to solve the dynamic optimization problem, which has infinite-dimensional decision variables and constraints. Without discretizing the UAV's trajectory, our algorithm maintains trajectory continuity and smoothness by discretizing only the decision variables. Moreover, the exact penalty function is adopted to handle the infinite-dimensional state constraints.

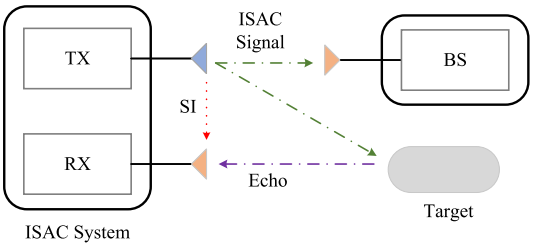

Fig. 3. An illustration of the ISAC transceiver.

- In the numerical simulations, the proposed UAV-ISAC approach, the benchmark BS-ISAC scheme, and an existing design method are utilized to detect targets with different moving speeds. The simulation results indicate that a significant enhancement in sensing performance with the UAV-ISAC approach compared to the BS-ISAC scheme. In addition, the results show that the performance of the existing method in real UAV systems falls short of its designed performance, exhibiting degradation in comparison to the proposed method.

II. System Description and Problem Definition

We consider a UAV-ISAC system as depicted in Fig. 2, where a quadrotor UAV is used to track and monitor a non-cooperative moving target. Besides the ISAC system, we assume that the UAV is also equipped with an optical camera to provide additional visual sensing information.

Fig. 3 depicts the ISAC system, comprising a transmit antenna (TX) and a receive antenna (RX), such that it has the full-duplex (FD) transceiver capability [25]. In the ISAC system, the TX transmits the wireless signal, whereas the RX receives the echo signal and extracts the sensing information of the target. To mitigate the impact of self-interference (SI), we separates the RX and the TX for passive suppression, followed by active cancellation strategies in analog and digital domains to further reduce SI levels [25]. Nonetheless, residual SI (RSI) that cannot be entirely eliminated persists in the echo signals at the RX. Furthermore, the high-speed UAV rotor rotation affects the electromagnetic field surrounding the antenna [26], thereby influencing the quality of the echo signals. In addition, the 6DoF motion of UAV affects both Doppler shift and Doppler power spectral density, and such influence can be complicated to model [27], [28]. However, in this paper, the potential impact of the UAV's rotor on wireless signal has not been taken into account. The Doppler induced by UAV's flight is assumed to be effectively compensated at both the BS [29], [30] and the sensing receiver [13], [31], [32].

In this scenario, we assume that the UAV already knows the accurate location of the BS in advance, and knows the real-time location of the target based on the existing location algorithm [33], [34], [35]. Let $\boldsymbol{x}_B = [x_B, y_B, z_B]^\top$ denote the location of the BS, where '$[\cdot]^\top$' stands for the transpose operation. At time t, the positions of the UAV and the target are represented by $\boldsymbol{q}(t) = [x(t), y(t), z(t)]^\top$ and $\boldsymbol{x}_T(t) = [x_T(t), y_T(t), z_T(t)]^\top$, respectively, with unit of meter. The objective is to optimize the 3D trajectory of the UAV to improve the sensing performance about the target. In what follows, we will introduce the key evaluation metrics and UAV dynamics model. For ease of reference, the essential symbols, their definitions, and associated units are presented in Table I.

TABLE I
Notations

Symbol	Definition	Unit
B	Channel bandwidth	MHz
C_t	Thrust coefficient	$\mathrm{N/(rad/s)^2}$
C_m	Torque coefficient	$\mathrm{N\cdot m/(rad/s)^2}$
C_{dx}	Drag coefficient for x-axis	$\mathrm{N/(m/s)^2}$
C_{dy}	Drag coefficient for y-axis	$\mathrm{N/(m/s)^2}$
C_{dz}	Drag coefficient for z-axis	$\mathrm{N/(m/s)^2}$
C_{dmx}	Damping torque coefficient for x-axis	$\mathrm{N\cdot m/(rad/s)^2}$
C_{dmy}	Damping torque coefficient for y-axis	$\mathrm{N\cdot m/(rad/s)^2}$
C_{dmz}	Damping torque coefficient for z-axis	$\mathrm{N\cdot m/(rad/s)^2}$
f_c	Carrier frequency	GHz
g	Gravitational acceleration	$\mathrm{m/s^2}$
G	UAV antenna gain	dBi
G_B	BS receiving antenna gain	dBi
h_{min}	Minimum flying height	m
h_{max}	Maximum flying height	m
I_x	Rotational inertia for x-axis	$\mathrm{kg\cdot m^2}$
I_y	Rotational inertia for y-axis	$\mathrm{kg\cdot m^2}$
I_z	Rotational inertia for z-axis	$\mathrm{kg\cdot m^2}$
I_m	Motor propeller inertia	$\mathrm{kg\cdot m^2}$
L	Fuselage radius	m
m	UAV mass	kg
P_c	ISAC communication transmit power	W
P_r	ISAC sensing transmit power	W
R_v	Video rate	Mbits/s
ω_{max}	Maximum motor speed	rad/s
ω_i	Speed of motor i	rad/s

A. Sensing Metric

To evaluate the sensing performance of the ISAC system, the amount of sensing MI [36], [37], [38], [39], [40] is recommended as the performance metric, which has the advantage that communication and sensing can be compared in the same dimension. The MI measures the maximum information rate of the ISAC echo signal from the target that can be reliably received by the UAV [41]. Based on information theory, a higher MI indicates an increased ability to derive information about the target through measurements [41]. The received baseband signal of the UAV-ISAC system is given by

$$r(t) = \sqrt{P_r(t-\tau_t)}s(t-\tau_t)h_r(t-\tau_t) + s_I(t) + n(t), \quad (1)$$

where $P_r(t)$ is the transmission power, $s(t)$ is the sensing signal with $\mathbb{E}[|s(t)|^2] = 1$, $h_r(t)$ is the double cascaded channel between the UAV and the target, τ_t is the time delay between transmitting the ISAC signal and receiving the echo signal back from the target, $s_I(t)$ is the RSI after SI cancellation, and $n(t)$ is a Gaussian noise signal with no bias and a power determined by the variance σ_n^2. From (1), the system sensing ability measured by the MI metric is given below [41], [42], [43]

$$\begin{aligned} I\left(y(t),\ h_r(t)\right) &= H(y(t)) - H(n(t)) \\ &= \rho B \log_2\left(1 + \mathrm{SINR_r}\right), \end{aligned} \quad (2)$$

where ρ is the proportion of the sensing signal in the ISAC signal, $H(\cdot)$ is the information entropy, B is the ISAC system bandwidth, $\mathrm{SINR_r}$ is the signal-to-interference-noise ratio

(SINR) of the received echo signal, which can be expressed as

$$\begin{aligned}\mathrm{SINR_r} &= \frac{\mathbb{E}[|\sqrt{P_r(t-\tau_t)}s(t-\tau_t)h_r(t-\tau_t)|^2]}{\mathbb{E}[|s_I(t)|^2]+\mathbb{E}[|n(t)|^2]} \\ &\approx \frac{P_r(t)\mathbb{E}\left[|h_r(t)|^2\right]}{\sigma_s^2+\sigma_n^2}. \end{aligned} \tag{3}$$

The term $\mathbb{E}[|\sqrt{P_r(t-\tau_t)}s(t-\tau_t)h_r(t-\tau_t)|^2]$ can be approximated as $\mathbb{E}[|\sqrt{P_r(t)}s(t)h_r(t)|^2]$, since the time delay τ_t is merely a few microseconds, which is too short to cause a notable variation. The RSI is modeled as zero-mean additive white Gaussian noise (AWGN) [25], and its impact on the SINR is quantified by the variance σ_s^2. The noise variance is given by $\sigma_n^2 = k_B T_{\text{temp}} B$, where $k_B = 1.38 \times 10^{-23}\mathrm{J/K}$ is the Boltzmann constant and T_{temp} is the absolute temperature. The non-cooperative channel gain can be obtained by [44]

$$\mathbb{E}\left[|h_r(t)|^2\right] = \frac{G^2\lambda^2\sigma_{\text{cross}}}{(4\pi)^3\left(d_R(t)\right)^4}, \tag{4}$$

where G is the UAV antenna gain (assuming that the transmitting and receiving antennas have the same gain), $\lambda = c/f_c$ is the carrier wavelength, f_c is carrier frequency, $c = 3\times10^8\mathrm{m/s}$ is the speed of light in vacuum, σ_{cross} is the target cross section area, and $d_R(t) = \|\boldsymbol{q}(t) - \boldsymbol{x}_T(t)\|$ is the distance between the UAV and the target. Therefore, the sensing MI of the UAV-ISAC system is expressed as

$$R_r(t) = \rho B \log_2\left(1 + \frac{P_r(t)\lambda_r}{\|\boldsymbol{q}(t)-\boldsymbol{x}_T(t)\|^4}\right), \tag{5}$$

where

$$\lambda_r = \frac{G^2\lambda^2\sigma_{\text{cross}}}{(4\pi)^3\left(\sigma_s^2+\sigma_n^2\right)}. \tag{6}$$

B. UAV On-Board Camera Data Rate

The optical camera on the UAV generates stable image data with a constant frame rate. In theory, the image data rate can be calculated as follows [45]

$$R_{bps} = R_{fps} N_{bpf}, \tag{7}$$

where R_{bps} is the image data rate (bits/s), R_{fps} is the frame rate of the UAV on-board camera (frames per second, fps), and N_{bpf} is the number of bits per frame (bpf). In theory, the standard video frame rate is not less than 24 fps. In fact, 24 fps and 25 fps are the video frame rate standards adopted by most countries and regions [45], and there is only slight visual perception difference between the two frame rates. The amount of data required to transmit per frame of an image is related to image pixels and the pixel format. When the video format is determined, the camera data rate is a constant. Considering the influence of the video compression technology and communication coding technology, the transmission rate required after the image data is converted into the communication data is

$$R_v = \eta_{comp} R_{bps} / \eta_{code}, \tag{8}$$

where η_{comp} is the video compression ratio and η_{code} is the channel coding rate. In this manuscript, R_v is considered as a constant rate.

C. UAV Sensing Information Transmission

Generally speaking, the transceiver antenna of the BS is in a high altitude, and a good LoS channel can be easily established with the UAV. The UAV transmits information data to the BS with a data rate given by [43]

$$R_c(t) = (1-\rho)B\log_2\left(1 + \frac{P_c(t)\mathbb{E}[|h_c(t)|^2]}{\sigma_n^2}\right), \tag{9}$$

where $P_c(t)$ is communication transmission power, $h_c(t)$ is the communication channel between the UAV and the BS which follows the free-space path loss model and can be expressed as [44]

$$\mathbb{E}[|h_c(t)|^2] = \frac{GG_B\lambda^2}{(4\pi)^2\left(d_C(t)\right)^2}, \tag{10}$$

where G_B is the BS antenna gain and $d_C(t) = \|\boldsymbol{q}(t) - \boldsymbol{x}_B\|$ is the distance between the UAV and the BS. Let

$$\lambda_c = \frac{GG_B\lambda^2}{(4\pi)^2\sigma_n^2}, \tag{11}$$

then (9) can be rewritten as

$$R_c(t) = (1-\rho)B\log_2\left(1 + \frac{P_c(t)\lambda_c}{\|\boldsymbol{q}(t)-\boldsymbol{x}_B\|^2}\right). \tag{12}$$

In order to ensure that the sensing and camera data received by the UAV is successfully uploaded to the BS receiver, the communication rate of the UAV should be greater than the sum of the video data rate and the sensing MI. This constraint is given below [46], [47]

$$R_c(t) \geq R_r(t) + R_v. \tag{13}$$

D. Energy Model

The energy consumption of UAV includes propulsion power, communication transmission power, optical camera power and other equipment power. As derived in [17], the propulsion power of a quadrotor UAV is given by

$$P(t) = \sum_{i=1}^{4} P_i(t), \tag{14}$$

where $P_i(t) = c_4\omega_i^4(t) + c_3\omega_i^3(t) + c_2\omega_i^2(t) + c_1\omega_i(t) + c_0$ is power consumption of the ith motor, $i = \{1,2,3,4\}$, c_0, c_1, c_2, c_3, c_4 are constant parameters depending on the motor, $\omega_i(t)$ is the speed of the ith motor, $i \in \{1,2,3,4\}$, as illustrated in Fig. 4. The total energy consumption of the UAV can be expressed by

$$E(t) = \int_0^t \left(P(\tau) + P_r(\tau) + P_c(\tau) + P_o\right)\,\mathrm{d}\tau, \tag{15}$$

where P_o is an average power constant, which includes the power consumption of optical camera power and other necessary on-board equipment. The remaining battery energy of the UAV is given by

$$E_r(t) = E_{total} - E(t), \tag{16}$$

where E_{total} is the total available energy of the onboard battery of the UAV before the mission begins.

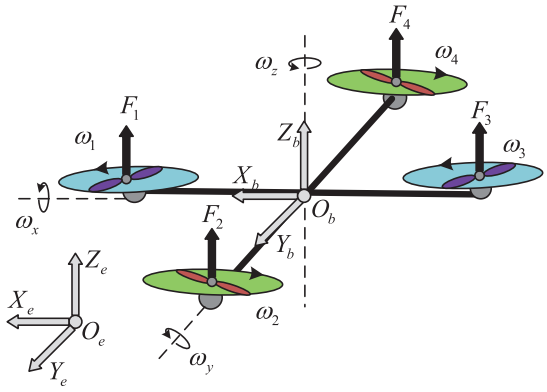

Fig. 4. The cartesian coordinate system of the UAV.

E. Rigid-Body Dynamic Model of Quad-Rotor UAV

In this manuscript, we consider the quadrotor UAV as a rigid body and study the influence of its rigid-body dynamics model on the trajectory. As illustrated in Fig. 4, the Earth frame and the fixed-body frame are defined as O_e and O_b, respectively. Let $\boldsymbol{q}(t)$ be the real-time position vector of the UAV at the Earth frame, and $\boldsymbol{\Omega}_b(t) = [\omega_x(t), \omega_y(t), \omega_z(t)]^\top$ be the UAV's angular velocity about the x-axis, y-axis, z-axis in the frame O_b at time t.

As shown in Fig. 4, the thrust $F_i(t),\ i \in \{1,2,3,4\}$ is generated by related electric motor: motors 1 and 3 counter-rotate, while motors 2 and 4 rotate clockwise with the angular velocity $\omega_i(t),\ i \in \{1,2,3,4\}$ as illustrated in Fig. 4. According to [16], the motors generate the thrusts $F_i(t) = C_t\omega_i^2(t)$, where C_t is the thrust coefficient.

Compared with the Euler angle-based representations for the rotational motion in prior work [17], unit quaternions are used to describe the UAV rotation motion in this manuscript. Thus, the UAV rotation does not need to satisfy the small disturbance hypothesis and the singularity problem caused by the Euler angle-based representations can be avoided. Let $\bar{\boldsymbol{q}}(t) = [q_0(t), q_1(t), q_2(t), q_3(t)]^\top$ denote unit quaternions, which satisfy $\|\bar{\boldsymbol{q}}(t)\| = 1$.

The control input vector $\boldsymbol{u}(t) = [u_1(t), u_2(t), u_3(t), u_4(t)]^\top$ is designed as [17]

$$\begin{aligned} u_1(t) &= \sum_{i=1}^{4} \omega_i^2(t), \\ u_2(t) &= \omega_2^2(t) - \omega_4^2(t), \\ u_3(t) &= \omega_3^2(t) - \omega_1^2(t), \\ u_4(t) &= \omega_1^2(t) - \omega_2^2(t) + \omega_3^2(t) - \omega_4^2(t). \end{aligned} \tag{17}$$

The motors' angular velocities are controlled by input control signal, and their analytical expression can be deduced from (17) as follows [17]

$$\begin{aligned} \omega_1(t) &= 0.5\left(u_1(t) + u_4(t) - 2u_3(t)\right)^{0.5}, \\ \omega_2(t) &= 0.5\left(u_1(t) - u_4(t) + 2u_2(t)\right)^{0.5}, \\ \omega_3(t) &= 0.5\left(u_1(t) + u_4(t) + 2u_3(t)\right)^{0.5}, \\ \omega_4(t) &= 0.5\left(u_1(t) - u_4(t) - 2u_2(t)\right)^{0.5}. \end{aligned} \tag{18}$$

The six-degree-of-freedom dynamic model of the UAV is given by (19), shown at the bottom of the next page, [48], where $\Omega(t) = \omega_1(t) - \omega_2(t) + \omega_3(t) - \omega_4(t)$, $\dot{x}(t)$ and $\ddot{x}(t)$ denote the first and second derivatives of variable x with respect to t, respectively. The physical meanings of the symbols are listed in Table I. And the quaternion propagation equations are shown below [49]

$$\dot{\bar{\boldsymbol{q}}}(t) = \frac{1}{2}\boldsymbol{\Omega}_q(t)\bar{\boldsymbol{q}}(t), \tag{20}$$

where

$$\boldsymbol{\Omega}_q(t) = \begin{bmatrix} 0 & -\omega_x(t) & -\omega_y(t) & -\omega_z(t) \\ \omega_x(t) & 0 & \omega_z(t) & -\omega_y(t) \\ \omega_y(t) & -\omega_z(t) & 0 & \omega_x(t) \\ \omega_z(t) & \omega_y(t) & -\omega_x(t) & 0 \end{bmatrix}.$$

Compared with the Euler angles used in [17], the quaternion method uses four elements to record the UAV attitude rotation, which is more complicated and not easy to understand intuitively. However, the quaternion method can avoid the singularity problem of attitude angle caused by the Euler method, and the computational cost is lower [50].

III. Problem Formulation

Based on the discussion of the model above, the JDCSC problem, which is a dynamic optimization problem based on the state-space model [51], is formulated in this section. For comparison, the existing design, which only consider the UAV kinematics with a fully discretized model, is utilized.

A. Dynamic Optimization Problem

In this paper, we assume that the target moves with uniform velocity V_T along the X_e-axis, the kinematic model of the target can be expressed as

$$\begin{aligned} \dot{x}_T(t) &= V_T, \\ \dot{y}_T(t) &= 0, \\ \dot{z}_T(t) &= 0. \end{aligned} \tag{21}$$

Acc state-space model [51], the state vector is defined as

$$\begin{aligned} \boldsymbol{x}(t) = [&x(t), y(t), z(t), v_x(t), x_T(t), v_y(t), v_z(t), \omega_x(t), \\ &\omega_y(t), \omega_z(t), q_0(t), q_1(t), \\ &q_2(t), q_3(t), E_r(t), Q_c(t), Q_r(t)]^\top, \end{aligned}$$

where $Q_c(t) = \int_0^t R_c(\tau)\mathrm{d}\tau$ is the theoretical cumulative throughput of the transmitted communication data from 0 to t and $Q_r(t) = \int_0^t R_r(\tau)\mathrm{d}\tau$ is the accumulated amount of the sensing MI from 0 to t. Then, the state-space model of the system (5), (12), (16), (19) and (20), can be written as (22), shown at the bottom of the next page. To simplify notation, (22) is rewritten as

$$\dot{\boldsymbol{x}}(t) = \boldsymbol{f}\left(\boldsymbol{x}(t), \boldsymbol{u}(t), P_r(t), P_c(t)\right). \tag{23}$$

The UAV-ISAC dynamic trajectory optimization problem is formulated as $\mathbf{P1}$. In problem $\mathbf{P1}$, C_0 is the dynamic equations. C_1 is introduced to limit the total force and torque generated by the UAV motors and control the ISAC transmission power, where $U_{1,min}$, $U_{i,max}$ $i = 1,2,3,4$, and P_{max} are constant values. C_2 is to ensure that the task

completion time has realistic physical significance. $\boldsymbol{x}_0$ in C_3 is the initial value of $\boldsymbol{x}(0)$. Constraint C_4 safeguards the UAV by maintaining a safe altitude, where h_{min} and h_{max} are the minimum and maximum allowable altitude, respectively. C_5 is the communication requirement constraint, which ensures that the UAV can successfully transmit sensing and video data to the BS. To successfully complete the mission, the UAV must reach an end-point before depleting the planned onboard energy. Therefore, the residual energy at the terminal time should satisfy C_6. C_7 is the end-point position constraint, where $\boldsymbol{q}_F = [x_F, y_F, z_F]^\top$ is end-point position. If the sensing task does not specify a terminal location, we can optimize **P1** without the constraint C_7.

$$
\begin{aligned}
\mathbf{P1}: \quad & \max_{\boldsymbol{u}(t),P_r(t),P_c(t),T} \quad Q_r(T) = \int_0^T R_r(\tau)\mathrm{d}\tau \\
& s.t. \quad C_0: \ \dot{\boldsymbol{x}}(t) = \boldsymbol{f}\left(\boldsymbol{x}(t), \boldsymbol{u}(t), P_r(t), P_c(t)\right), \\
& \quad t \in [0, T], \\
& \quad C_1: \ U_{1,min} \le u_1(t) \le U_{1,max}, \\
& \quad |u_i(t)| \le U_{i,max}, \ i = 2, 3, 4, \\
& \quad 0 \le P_r(t) \le P_{max}, \\
& \quad 0 \le P_c(t) \le P_{max}, \ t \in [0, T], \\
& \quad C_2: \ T > 0, \\
& \quad C_3: \ \boldsymbol{x}(0) = \boldsymbol{x}_0, \\
& \quad C_4: \ h_{min} \le z(t) \le h_{max}, \ t \in [0, T], \\
& \quad C_5: \ R_c(t) \ge R_r(t) + R_v, \ t \in [0, T], \\
& \quad C_6: \ E_r(T) \ge 0, \\
& \quad C_7: \ x(T) = x_F, \\
& \qquad y(T) = y_F, \ z(T) = z_F.
\end{aligned}
$$

B. Existing Design

For existing design, the UAV is regarded as a mass point and only the kinematics of UAV are considered. Moreover, a fully discretized model is usually adopted. In this case, we use the UAV centroid velocity vector generated by the UAV motors as the decision variable, which is denoted as $\boldsymbol{v}[n] = [v_x[n], \ v_y[n], \ v_z[n]]^\top$. The discrete kinematic equation is described as [14], [15], and [13]

$$
\boldsymbol{q}[n+1] = \boldsymbol{q}[n] + \boldsymbol{v}[n]\Delta_t, \tag{24}
$$

where Δ_t is discrete time step. The motion power consumption of UAV can be estimated as follows [17]

$$
\begin{aligned}
P_\omega[n] = {} & C_{p1}\left(1 + C_{p2}\left(v_x^2[n] + v_y^2[n]\right)^2\right)^{\frac{3}{4}} + mgv_z[n] \\
& + C_{dz}|v_z[n]|^3 + P_o + P_r[n] + P_c[n],
\end{aligned} \tag{25}
$$

where $C_{p1} = 4C_m\left(\frac{mg}{4C_t}\right)^{\frac{3}{2}}$, $C_{p2} = \left(\frac{C_{dx}}{mg}\right)^2$.

Similarly to (5) and (12), the discrete sensing and communication rate can be expressed as follows

$$
R_r[n] = \rho B \log_2\left(1 + \frac{P_r[n]\lambda_r}{\|\boldsymbol{q}[n] - \boldsymbol{x}_T[n]\|^4}\right), \tag{26}
$$

$$
R_c[n] = (1-\rho) B \log_2\left(1 + \frac{P_c[n]\lambda_c}{\|\boldsymbol{q}[n] - \boldsymbol{x}_B\|^2}\right). \tag{27}
$$

$$
\begin{cases}
m\ddot{x}(t) = C_t u_1(t)\left(2\left(q_1(t)q_3(t) + q_0(t)q_2(t)\right)\right) - C_{dx}\dot{x}(t)|\dot{x}(t)|, \\
m\ddot{y}(t) = C_t u_1(t)\left(2\left(q_2(t)q_3(t) - q_0(t)q_1(t)\right)\right) - C_{dy}\dot{y}(t)|\dot{y}(t)|, \\
m\ddot{z}(t) = C_t u_1(t)\left(q_0(t)^2 - q_1(t)^2 - q_2(t)^2 + q_3(t)^2\right) - mg - C_{dz}\dot{z}(t)|\dot{z}(t)|, \\
I_x\dot{\omega}_x(t) = LC_t u_2(t) + (I_y - I_z)\omega_y(t)\omega_z(t) - I_m\Omega(t)\omega_y(t) - C_{dmx}\omega_x(t)\left|\omega_x(t)\right|, \\
I_y\dot{\omega}_y(t) = LC_t u_3(t) + (I_z - I_x)\omega_x(t)\omega_z(t) + I_m\Omega(t)\omega_x(t) - C_{dmy}\omega_y(t)\left|\omega_y(t)\right|, \\
I_z\dot{\omega}_z(t) = C_m u_4(t) + (I_x - I_y)\omega_x(t)\omega_y(t) - C_{dmz}\omega_z(t)\left|\omega_z(t)\right|,
\end{cases} \tag{19}
$$

$$
\begin{cases}
\dot{x}(t) = v_x(t), \ \dot{y}(t) = v_y(t), \ \dot{z}(t) = v_z(t), \ \dot{x}_T(t) = V_T, \\
\dot{v}_x(t) = \left[2C_t u_1(t)\left(q_1(t)q_3(t) + q_0(t)q_2(t)\right) - C_{dx}|v_x(t)|v_x(t)\right]/m, \\
\dot{v}_y(t) = \left[2C_t u_1(t)\left(q_2(t)q_3(t) - q_0(t)q_1(t)\right) - C_{dy}|v_y(t)|v_y(t)\right]/m, \\
\dot{v}_z(t) = \left[C_t u_1(t)\left(q_0(t)^2 - q_1(t)^2 - q_2(t)^2 + q_3(t)^2\right) - mg - C_{dz}|v_z(t)|v_z(t)\right]/m, \\
\dot{\omega}_x(t) = \left[LC_t u_2(t) + (I_y - I_z)\omega_y(t)\omega_z(t) - I_m\Omega(t)\omega_y(t) - C_{dmx}|\omega_x(t)|\omega_x(t)\right]/I_x, \\
\dot{\omega}_y(t) = \left[LC_t u_3(t) + (I_z - I_x)\omega_x(t)\omega_z(t) + I_m\Omega(t)\omega_x(t) - C_{dmy}|\omega_y(t)|\omega_y(t)\right]/I_y, \\
\dot{\omega}_z(t) = \left[C_m u_4(t) + (I_x - I_y)\omega_x(t)\omega_y(t) - C_{dmz}|\omega_z(t)|\omega_z(t)\right]/I_z, \\
\dot{q}_0(t) = 0.5\left[-\omega_x(t)q_1(t) - \omega_y(t)q_2(t) - \omega_z(t)q_3(t)\right], \\
\dot{q}_1(t) = 0.5\left[\omega_x(t)q_0(t) + \omega_z(t)q_2(t) - \omega_y(t)q_3(t)\right], \\
\dot{q}_2(t) = 0.5\left[\omega_y(t)q_0(t) - \omega_z(t)q_1(t) + \omega_x(t)q_3(t)\right], \\
\dot{q}_3(t) = 0.5\left[\omega_z(t)q_0(t) + \omega_y(t)q_1(t) - \omega_x(t)q_2(t)\right], \\
\dot{E}_r(t) = -\sum_{i=1}^{4} P_i(t) - P_r(t) - P_c(t) - P_o, \\
\dot{Q}_c(t) = (1-\rho)B\log_2\left(1 + \frac{P_c(t)\lambda_c}{\|\boldsymbol{q}(t) - \boldsymbol{x}_B\|^2}\right) \ \dot{Q}_r(t) = \rho B\log_2\left(1 + \frac{P_r(t)\lambda_r}{\|\boldsymbol{q}(t) - \boldsymbol{x}_T(t)\|^4}\right).
\end{cases} \tag{22}
$$

Similar to **P1**, the optimization problem for the UAV, in which the UAV is regarded as a mass point, can be formulated as

$$
\begin{aligned}
\mathbf{P2}: \quad & \max_{\boldsymbol{v}[n],P_r[n],P_c[n],\Delta_t} \quad \sum_{n=1}^{N} R_r[n] \\
& s.t. \quad S_0: \ \boldsymbol{q}[n+1]=\boldsymbol{q}[n]+\boldsymbol{v}[n]\Delta_t, \\
& \quad n\in\{1,2,\cdots,N\}, \\
& \quad S_1: \ \|\boldsymbol{v}[n]\|\le V_{max}, \\
& \quad 0\le P_r[n]\le P_{max}, \\
& \quad 0\le P_c[n]\le P_{max}, \ n\in\{1,2,\cdots,N\}, \\
& \quad S_2: \ \Delta_t>0, \\
& \quad S_3: \ \boldsymbol{q}[1]=\boldsymbol{q}_0, \\
& \quad S_4: \ \boldsymbol{q}[N+1]=\boldsymbol{q}_F, \\
& \quad S_5: \ h_{min}\le z[n]\le h_{max}, \\
& \quad n\in\{1,2,\cdots,N\} \\
& \quad S_6: \ R_c[n]\ge R_r[n]+R_v, \\
& \quad n\in\{1,2,\cdots,N\} \\
& \quad S_7: \ \sum_{n=1}^{N} P_\omega[n]\le E_{total}, \\
& \quad n\in\{1,2,\cdots,N\}
\end{aligned}
$$

where N is the total number of time slots.

IV. Proposed Solution Method

A. Preliminary Treatment

In this subsection, the optimal solution of $P_c(t)$ in problem **P1** is analytically derived, which yields a closed form expression for $P_c(t)$ in C_5 and highly simplifies the computation burden.

Theorem 1: The communication throughput monotonically increases with $P_c(t)$. When $P_c(t)$ is in the lower bound, the power consumption of communication is minimum. The optimal value of $P_c^*(t)$ is obtained as follows:

$$
\begin{aligned}
P_c^*(t) &= f_p\left(\boldsymbol{q}(t),P_r(t),\boldsymbol{x}_T(t)\right) \\
&\triangleq \left[(1+\mathrm{SINR_r})^{\frac{\rho}{1-\rho}}2^{r_v}-1\right]\frac{\|\boldsymbol{q}(t)-\boldsymbol{x}_B(t)\|^2}{\lambda_c} \\
& s.t. \quad f_p\left(\boldsymbol{q}(t),P_r(t),\boldsymbol{x}_T(t)\right)\le P_{max}
\end{aligned}
$$

where $\mathrm{SINR_r}=\frac{\lambda_r P_r(t)}{\|\boldsymbol{q}(t)-\boldsymbol{x}_T(t)\|^4}$ *and* $r_v=R_v/\left(B(1-\rho)\right)$.

Proof: See Appendix A. □

B. Control Parameterization Method

It is challenging to solve dynamic optimization problem **P1**. For example, (C_0) are dynamical constraints, and (C_4, C_5) are infinite-dimensional constraints. Firstly, a time-scaling transform is utilized [52] to map the varying time domain into a fixed S-domain; Secondly, the control parameterization method [53] is adopted to parametrize the infinite-dimensional decision variables into a finite vector. Thirdly, an exact penalty function method [54] to append the infinite-dimensional state inequality constraints and terminal state equality constraints. The proposed method is also applicable to task scenarios without the terminal location constraint (C_7).

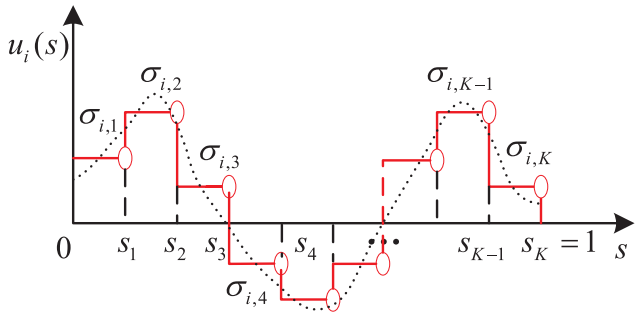

Fig. 5. Control parametrization.

C. Time-Scaling Transform and Control Parametrization

The linear transform is utilized in problem **P1** for mapping the time interval $[0,T]$ into a known S-domain $s\in[0,1]$ [52]:

$$\frac{\mathrm{d}t}{\mathrm{d}s}=T. \tag{28}$$

Based on (28), using the chain derivative rule, we can obtain the differential equation of (23) in the S-domain as [52]

$$\dot{\boldsymbol{x}}(s)=\frac{\mathrm{d}\boldsymbol{x}}{\mathrm{d}t}\frac{\mathrm{d}t}{\mathrm{d}s}=T\cdot\boldsymbol{f}\left(\boldsymbol{x}(s),\boldsymbol{u}(s),P_r(s),P_c(s)\right). \tag{29}$$

As shown in Fig. 5, the S-domain interval $[0,1]$ is divided into K equal subintervals with the $K+1$ points $s_k=k/K$, $k\in\mathbb{K}=\{0,1,\cdots,K-1,K\}$. For each control variable $u_i(s)$, $i\in\{1,2,3,4\}$ and $P_r(s)$, the variables are approximated by

$$u_i(s)\approx\sum_{k=1}^{K}\sigma_{i,k}\mathcal{F}_{[s_{k-1},s_k)}(s), \tag{30}$$

$$P_r(s)\approx\sum_{k=1}^{K}\sigma_{5,k}\mathcal{F}_{[s_{k-1},s_k)}(s), \tag{31}$$

where

$$\mathcal{F}_{[s_{k-1},s_k)}(s)=\begin{cases}1, & s\in[s_{k-1},s_k),\\ 0, & \text{otherwise.}\end{cases}$$

By letting $\boldsymbol{\sigma}_i=[\sigma_{i,1},\sigma_{i,2},\ldots,\sigma_{i,K}]^\top$, $i\in\{1,2,3,4,5\}$ and $\boldsymbol{\sigma}=\left[\boldsymbol{\sigma}_1^\top,\boldsymbol{\sigma}_2^\top,\boldsymbol{\sigma}_3^\top,\boldsymbol{\sigma}_4^\top,\boldsymbol{\sigma}_5^\top\right]^\top$, $\boldsymbol{u}(s)$ and $P_r(s)$ are thus parameterized by vector $\boldsymbol{\sigma}$. By replacing $\boldsymbol{u}(s)$ and $P_r(s)$ with $\boldsymbol{\sigma}$, (29) become

$$\dot{\boldsymbol{x}}(s)=T\cdot\boldsymbol{f}\left(\boldsymbol{x}(s),\boldsymbol{\sigma},P_c(s)\right). \tag{32}$$

Therefore, we obtain the following problem $(\mathbf{P1})_\sigma$:

$$
\begin{aligned}
(\mathbf{P1})_\sigma: \quad & \min_{\boldsymbol{\sigma},T} \quad -Q_r(1) \\
& s.t. \quad \mathcal{C}_0: \ \dot{\boldsymbol{x}}(s)=T\cdot\boldsymbol{f}\left(\boldsymbol{x}(s),\boldsymbol{\sigma},P_c(s)\right), \\
& \quad s\in[0,1], \\
& \quad \mathcal{C}_1: \ U_{1,min}\le\sigma_{1,k}\le U_{1,max}, \\
& \quad |\sigma_{i,k}|\le U_{i,max}, \ i=2,3,4, \\
& \quad 0\le\sigma_{5,k}\le P_{max}, k\in\mathbb{K}, \\
& \quad \mathcal{C}_2: \ T>0, \\
& \quad \mathcal{C}_3: \ \boldsymbol{x}(0)=\boldsymbol{x}_0,
\end{aligned}
$$

$$
\begin{aligned}
&\mathcal{C}_4:\ h_{min} \le z(s) \le h_{max},\ s \in [0,1],\\
&\mathcal{C}_5:\ P_c(s) = f_p\left(\boldsymbol{q}(s),\right.\\
&\left.\sigma_{5,k}, \boldsymbol{x}_T(s)\right),\ s \in [0,1],\\
&\mathcal{C}_6:\ E_r(1) \ge 0,\\
&\mathcal{C}_7:\ x(1) = x_F,\ y(1) = y_F,\ z(1) = z_F,\\
&\mathcal{C}_8:\ f_p\left(\boldsymbol{q}(s), \sigma_{5,k}, \boldsymbol{x}_T(s)\right)\\
&\le P_{max},\ s \in [0,1].
\end{aligned}
$$

D. Exact Penalty Function Scheme

According to [53] and [54], the terminal equality constraint of $\mathcal{C}_7$ is converted into the following form:

$$\Delta_e = \epsilon^{-\alpha}\left[\left(x(1)-x_F\right)^2 + \left(y(1)-y_F\right)^2 + \left(z(1)-z_F\right)^2\right], \tag{33}$$

where $\alpha > 0$ is a penalty weight exponential constant. The terminal inequality constraint of $\mathcal{C}_6$ is converted into the following form:

$$\Delta_{ine} = \epsilon^{-\alpha}\min\left\{0,\ E_r(1) + \epsilon^{\beta} W_0\right\}^2, \tag{34}$$

where $\beta > 0$ is a positive real number, W_0 is a constant positive weight. Similarly, $\mathcal{C}_4$ and $\mathcal{C}_8$ are transformed into the following alternative:

$$
\begin{aligned}
\Delta_i = \epsilon^{-\alpha}\Big[&\min\left\{0,\ z(s) - h_{min} + \epsilon^{\beta} W_1\right\}^2\\
&+ \min\left\{0,\ h_{max} - z(s) + \epsilon^{\beta} W_1\right\}^2\\
&+ \min\left\{0,\ P_{max} - f_p\left(\boldsymbol{q}(s), \sigma_{5,k}, \boldsymbol{x}_T(s)\right) + \epsilon^{\beta} W_2\right\}^2\Big],
\end{aligned} \tag{35}
$$

where W_1 and W_2 are fixed constants.

Therefore, the problem $(\mathbf{P1})_{\sigma}$ can be transformed into the optimal control problem $(\mathbf{P1})_{\sigma,\epsilon}$ without state constraints:

$$
\begin{aligned}
(\mathbf{P1})_{\sigma,\epsilon}: \min_{\boldsymbol{\sigma},T,\epsilon}\ & J = -Q_r(1) + \delta\epsilon^{\gamma} + \Delta_e + \Delta_{ine} + \int_0^1 \Delta_i \mathrm{d}s\\
s.t.\ \ & \mathcal{C}_0,\ \mathcal{C}_1,\ \mathcal{C}_2,\ \mathcal{C}_3,\ \mathcal{C}_5,\\
& \mathcal{C}_9:\ \epsilon > 0,
\end{aligned}
$$

where $\gamma \ge 2$ and $\delta > 0$ are penalty parameters. Note that problem $(\mathbf{P1})_{\sigma,\epsilon}$ can be treated as a standard nonlinear program problem without state constraints. The key steps involved in solving problem $(\mathbf{P1})_{\sigma}$ outlined in Algorithm 1.

E. Gradient Formulas

To solve the nonlinear programming problem $(\mathbf{P1})_{\sigma,\epsilon}$ in Algorithm 2, we need to derive the gradient formulas of the objective function J with respect to $\boldsymbol{\sigma}$, T, and ϵ. The gradient formulas for the objective function of $(\mathbf{P1})_{\sigma,\epsilon}$ are given in the following Theorem 2.

Theorem 2: The gradients of the objective function J with respect to $\boldsymbol{\sigma}$, T, and ϵ are given by

$$\frac{\partial J}{\partial \boldsymbol{\sigma}} = \int_0^1 \frac{\partial H}{\partial \boldsymbol{\sigma}}\mathrm{d}s,$$

Algorithm 1 Optimization Algorithm of Problem $(\mathbf{P1})_{\sigma}$

Initialization: Set $\delta^{(1)} = 10$, $\epsilon^{(1)} = 0.1$, $\epsilon^{*} = 10^{-5}$, the iteration index $iter = 1$. The penalty parameter values α, β, γ, and W_i, $= 0, 1, 2$, are chosen depending on the problem $(\mathbf{P1})_{\sigma,\epsilon}$.
1: **while** $\epsilon^{(iter)} > \epsilon^{*}$ and $\delta^{(iter)} < 10^8$:
2: Solving $(\mathbf{P1})_{\sigma,\epsilon}$ based on Algorithm 2 with the initial point $\left(\boldsymbol{\sigma}^{(iter)}, T^{(iter)}, \epsilon^{(iter)}\right)$, and the locally optimal result $\left(\boldsymbol{\sigma}^{(iter),*}, T^{(iter),*}, \epsilon^{(iter),*}\right)$ is obtained.
3: **if** All constraints are satisfied:
4: **break**.
5: **else**:
6: Adjust α, β, γ, and set $\epsilon^{(iter),*} = 0.1\epsilon^{(iter)}$, $\delta^{(iter)} = 0.1\delta^{(iter)}$
7: **end if**
8: Let $\delta^{(iter+1)} = 10\delta^{(iter)}$, $\boldsymbol{\sigma}^{(iter+1)} = \boldsymbol{\sigma}^{(iter),*}$, $T^{(iter+1)} = T^{(iter),*}$, $\epsilon^{(iter+1)} = \epsilon^{(iter),*}$, $iter = iter + 1$.
9: **end while**
10: **Output**: $\left(\boldsymbol{\sigma}^{(iter),*}, T^{(iter),*}\right)$.

Algorithm 2 Solving Problem $(\mathbf{P1})_{\sigma,\epsilon}$ at Iteration j

Input: $\boldsymbol{\sigma}^{(j)}$, $T^{(j)}$, and $\epsilon^{(j)}$.
Output: $\boldsymbol{\sigma}^{(j+1)}$, $T^{(j+1)}$, and $\epsilon^{(j+1)}$.
1: Approximate $\boldsymbol{u}^{(j)}(s)$ with $\boldsymbol{\sigma}^{(j)}$ based on (30).
2: Solve $\dot{\boldsymbol{x}}^{(j)}(s) = T^{(j)}\boldsymbol{f}\left(\boldsymbol{x}^{(j)}(s), \boldsymbol{\sigma}^{(j)}, P_c(s)\right),\ s \in [0,1]$ for $\boldsymbol{x}^{(j)}(s)$ with $\boldsymbol{x}(0) = \boldsymbol{x}_0$, $\boldsymbol{\sigma}^{(j)}$, and $T^{(j)}$.
3: Calculate the objective function's gradients with $\boldsymbol{x}^{(j)}(s)$, $\boldsymbol{\sigma}^{(j)}$, $T^{(j)}$, and $\epsilon^{(j)}$.
4: Provide the objective function's values and gradients to the SQP-based nonlinear program solver.
5: Output $\boldsymbol{\sigma}^{(j+1)}$, $T^{(j+1)}$, and $\epsilon^{(j+1)}$.

$$
\begin{aligned}
\frac{\partial J}{\partial T} &= \int_0^1 \frac{\partial H}{\partial T}\mathrm{d}s,\\
\frac{\partial J}{\partial \epsilon} &= \delta\gamma\epsilon^{\gamma-1} - \alpha\epsilon^{-\alpha-1}\left(\Delta_e + \Delta_{ine} + T\int_0^1 \Delta_i \mathrm{d}s\right)\\
&\quad + 2\beta\epsilon^{\beta-\alpha-1}T\int_0^1 \Big[W_1\min\left\{0,\ x_3(s) - h_{min} + \epsilon^{\beta}W_1\right\}\\
&\quad + W_1\min\left\{0,\ h_{max} - x_3(s) + \epsilon^{\beta}W_1\right\}\\
&\quad + W_2\min\left\{0,\ P_{max} - f_p(s) + \epsilon^{\beta}W_2\right\}\Big]\mathrm{d}s
\end{aligned}
$$

respectively, where H is the Hamiltonian function formulated as

$$H = \Delta_i + T\boldsymbol{\lambda}(s)^{\top}\boldsymbol{f}\left(\boldsymbol{x}(s), \boldsymbol{\sigma}, P_c(s)\right) \tag{36}$$

and $\boldsymbol{\lambda}(s)$ is given by the following differential equation

$$\dot{\boldsymbol{\lambda}}(s) = -\frac{\partial H}{\partial \boldsymbol{x}}^{\top} \tag{37}$$

with

$$\boldsymbol{\lambda}(1) = \frac{\partial\left(-x_{16}(1) + \Delta_e + \Delta_{ine}\right)}{\partial \boldsymbol{x}}^{\top}. \tag{38}$$

Proof: See Appendix B. □

TABLE II
SOME PARAMETERS OF THE UAV-ISAC SYSTEM [17], [43]

m	3	c_0	3.6×10^{-3}	C_t	4.848×10^{-5}
g	9.8	c_1	7.5×10^{-4}	C_m	8.891×10^{-7}
L	0.3	c_2	8.5938×10^{-6}	C_{dmx}	0.016
B	10	c_3	8.8949×10^{-7}	C_{dmy}	0.016
P_{max}	1	c_4	5.1287×10^{-10}	C_{dmz}	0.1
P_o	9	C_{dx}	0.11	I_x	4.29×10^{-2}
h_{min}	60	C_{dy}	0.11	I_y	4.29×10^{-2}
h_{max}	200	C_{dz}	0.2	I_z	7.703×10^{-2}
R_v	40	ω_{max}	640	I_m	8.02×10^{-4}
G	17	G_B	20	f_c	28

F. Convergence Analysis and Computational Complexity

In the initial optimization stage, to relax penalties for constraint violations, the optimizer can start with a large ϵ to reduce penalty weight and relax constraints. As violations decrease, ϵ can be reduced to increase penalty weight and tighten constraints, further reducing violations. Decreasing ϵ reduces penalties $\delta\epsilon^{\gamma}$, leading to cost function reduction. Based on section 9.3.2 of [53], if the parameter $iter$ is sufficiently large ($iter \to \infty$), then $\epsilon^{(iter)} \to 0$, $\left(\boldsymbol{\sigma}^{(iter),*}, T^{(iter),*}\right) \to \left(\boldsymbol{\sigma}^{*}, T^{*}\right)$ is a local minimizer of Problem $\mathbf{P1}$. Thus, Algorithm 1 is convergent.

We use the SQP method [55], [56] to solve the nonlinear programming problem $(\mathbf{P1})_{\sigma,\epsilon}$ in Algorithm 2. The computational complexity of Algorithm 2 is $O\left((5K+2)^2\right)$, where K is usually assigned as 10. Because the improvement in the performance of the problem $(\mathbf{P1})_{\sigma,\epsilon}$ is marginal if $K > 10$ [17]. However, the algorithms outlined in [13], which regard UAV as points for trajectory optimization, exhibit a computational complexity of $O\left((5N)^{3.5}\right)$, where $N = 400$ is the number of time slots. It is noteworthy that this paper models the UAV as a rigid body, increasing the number of UAV state variables. However, by focusing on optimizing control inputs rather than state variables directly, we have successfully circumvented the increase in computational complexity that would arise from a sharp increase in the number of state variables. Furthermore, the control parameterization employed in this paper achieves a smooth UAV trajectory with a few control parameters, contrasting with [13] that requires many time slots for a refined trajectory, leading to reduced computational demand.

V. SIMULATION RESULTS

In the simulation, we consider a UAV-ISAC system where the UAV flies from the start point $\boldsymbol{q}_0 = [500,\ 2600,\ 100]^\top$ to the end point $\boldsymbol{q}_F = [0,\ 2600,\ 100]^\top$ before the given energy $E_{total} = 30$ kJ runs out. Meanwhile, the UAV collects information (including the ISAC signal and camera data) about a single target to the BS whose position is $\boldsymbol{x}_B = [0, 0, 30]^\top$. For ISAC, the proportion of sensing signal is $\rho = 0.5$. The ambient temperature and the target cross-sectional area are set to be $T_{temp} = 290$ K and $\sigma_{\text{cross}} = 2$ m^2, respectively. The RSI power is set as $\sigma_s^2 = -130$ dB [25]. Some parameters of the UAV-ISAC system are listed in Table II [17], [43]. The UAV initial conditions for problem $\mathbf{P1}$ are set as $\boldsymbol{x}_0 = [\boldsymbol{q}_0^\top,\ x_T(0),\ 0,\ 0,\ 0,\ 0,\ 0,\ 0,\ 1,\ 0,\ 0,\ 0,\ E_{total},\ 0,\ 0]^\top$. The maximum velocity of the UAV in problem $\mathbf{P2}$ is set as 20 m/s.

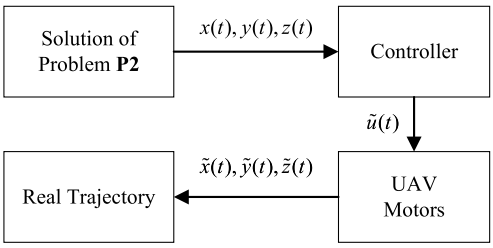

Fig. 6. The flowchart of obtaining the real trajectory of $\mathbf{P2}$.

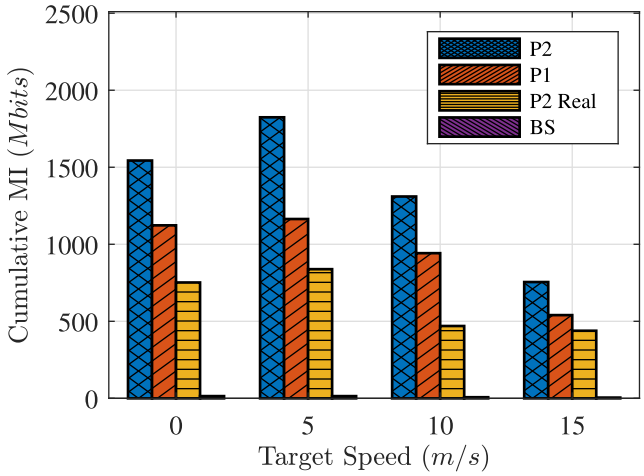

Fig. 7. The cumulative MI comparison with different target speeds.

Problem $\mathbf{P2}$ can be solved by on-the-shelf nonlinear program packages and then the planned trajectory are tracked by the UAV controller. The procedure for obtaining the real trajectory with existing design is shown in Fig. 6. In the event that constraint (13) is not satisfied, the sensing data transmission is deemed unsuccessful.

We consider two scenarios. In the first scenario, a stationary target is considered with position $\boldsymbol{x}_T = [250,\ 3000,\ 0]^\top$. The other scenario considers a moving target with the start point at $\boldsymbol{x}_T(0) = [500,\ 3000,\ 0]^\top$ and a uniform velocity V_T along the X-axis at 5 m/s, 10 m/s, and 15 m/s, respectively. We choose the penalty parameter $\alpha = 1.5$, $\beta = 2$, $\gamma = 3$ [54] and $W_0 = W_1 = W_2 = 10$ in the problem $(\mathbf{P1})_{\sigma,\epsilon}$ based on Algorithm 1. As described in Algorithm 1, the value of the penalty parameter can be adjusted for better constraint satisfaction.

A benchmark scheme with only BS sensing is used for comparison. In this scheme, the BS is equipped with a FD-ISAC system, which is called BS-ISAC. The transmitting antenna transmits the ISAC signal, and the receiving antenna receives the echo signal reflected back by the target. The perceived MI of the target obtained by the BS-ISAC system can be calculated by the following formula

$$R_b(t) = B\log_2\left(1 + \frac{P_B G_B^2 \lambda^2 \sigma_{\text{cross}}}{(4\pi)^3(\sigma_s^2 + \sigma_n^2)\|\boldsymbol{x}_T(t) - \boldsymbol{x}_B\|^4}\right), \tag{39}$$

where $P_B = 50$ W is the BS transmission power. For a stationary target, the focus is on the cumulative sensing MI acquired within 200 seconds of perception time. In the case

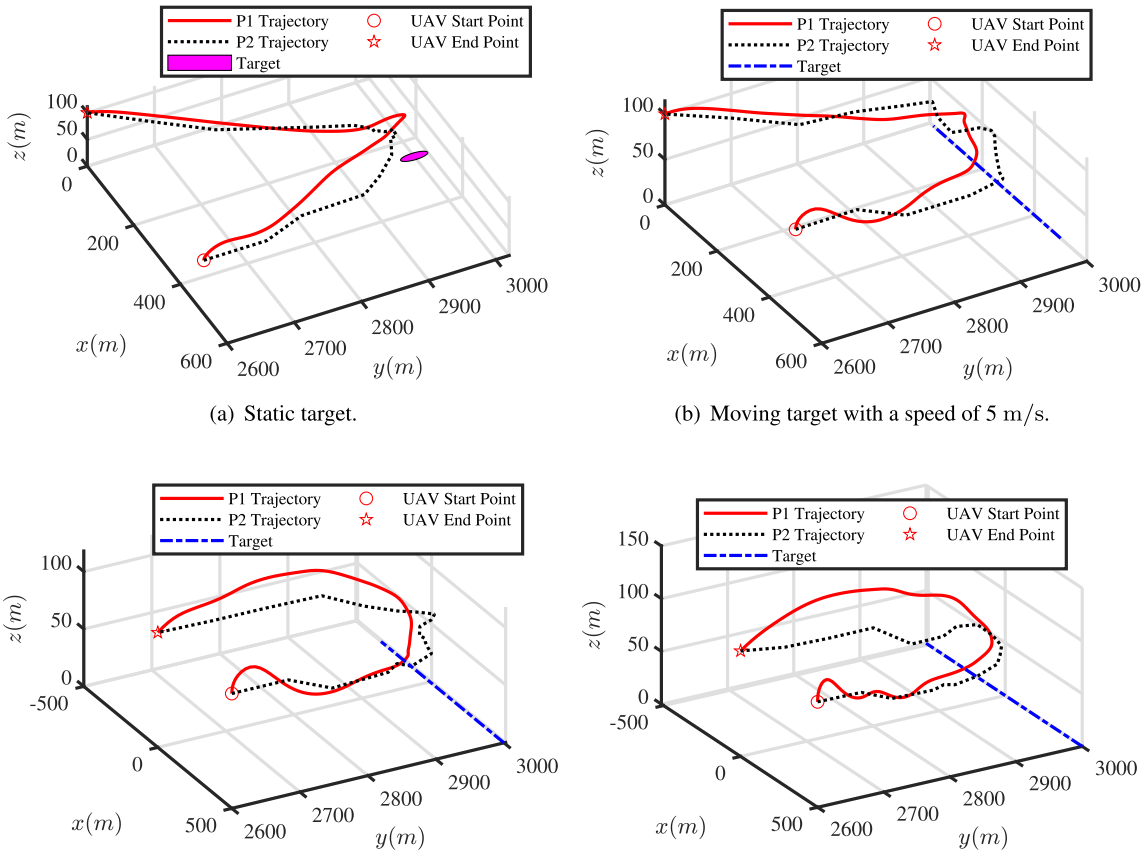

(a) Static target.

(b) Moving target with a speed of 5 m/s.

(c) Moving target with a speed of 10 m/s.

(d) Moving target with a speed of 15 m/s.

Fig. 8. The trajectories of the UAV and target.

of a moving target, the sensing outcomes within the $x_T(t) \in [-500, 500]$ segment of the X-axis are taken into account.

The cumulative MI of the BS-ISAC, **P1**, **P2**, and **P2** with real trajectory (P2 Real) are plotted in Fig. 7. As shown in Fig. 7, we observe that as the target's speed increases from 5 m/s to 15 m/s, the MI obtained by both the BS and the UAV gradually decreases. The faster the target moves, the shorter the time it spends within the perceptible section of the BS-ISAC system, leading to a decrease in the total sensing MI. For the UAV-ISAC system, the faster speed of the target, the quicker the UAV needs to approach the target, resulting in faster energy consumption and less sensing MI of the target. As expected, although P2 outperforms P1, the performance of the P2 Real is not as good as P1, which is clearly illustrated in Fig. 7. This further verifies that the ignoring the UAV dynamics may lead to performance degradation.

The flying trajectories and real time ISAC date rate of P1 and P2 are plotted in Fig. 8 and Fig. 9, respectively. As shown in Fig. 8 and Fig. 9, both of the trajectories and the ISAC data rate of the two methods look similar. At the beginning, the UAV flies in the direction close to the target to obtain better sensing performance. Limited by the communication capacity, the UAV maintains a stable sensing distance between the UAV and the target to ensure that the communication rate is no less than the sensing rate. As the UAV's onboard energy runs out, the UAV starts flying towards the end point and away from the target, resulting in a gradual decrease in the ISAC rate, ultimately reaching the destination before the energy is completely depleted. As shown in Fig. 9, when the velocity of the target increases, the UAV has less time to maintain peak ISAC rates. Consequently, the UAV must swiftly track the moving target, leading to increased energy consumption. In order to reach the destination before energy depletion, the UAV must balance its time moving away from the target.

However, the planned UAV trajectory of P2, as shown in Fig. 6, is required to be tracked by the controller. Thus, we plot both the planned UAV trajectories and the real UAV trajectories of P2 in Fig. 10. As shown in Fig. 10, the planned trajectories of P2 are not fully tracked. This deviation happened because the UAV's dynamic characteristics are not considered during the planning the of trajectory of P2, resulting in some segments of the planned trajectory not align with the UAV's dynamic response. As a result, the controller could not achieve precise tracking of the planned trajectory. Furthermore, the UAV cannot reach the end point before the exhaustion of its battery power. Specifically, the energy consumption model for P2, based on the UAV controller in Fig. 6, underestimated the actual UAV electrical energy expenditure. In addition, the controller, while tracking the P2 planned trajectory, cannot implement an optimal energy consumption control throughout the entire task, leading to unnecessary energy dissipation. This wastage exacerbated the rate of onboard energy depletion, ultimately preventing the UAV from reaching the end point before energy depletion.

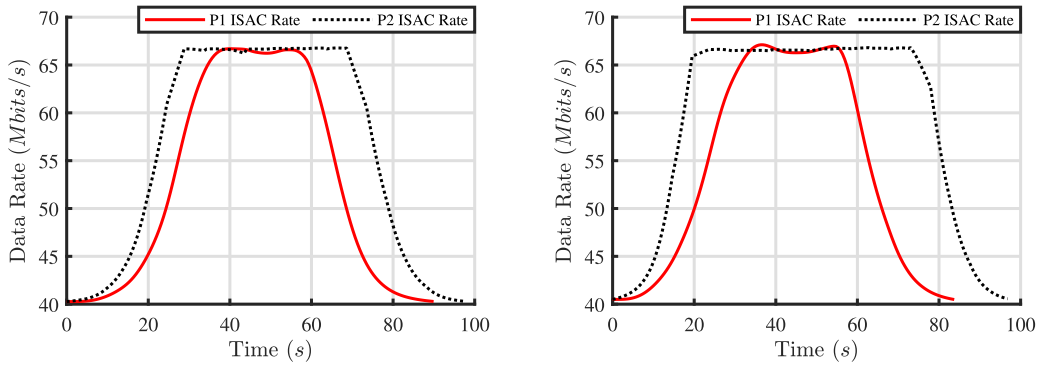

(a) Static target. (b) $V_T = 5$m/s.

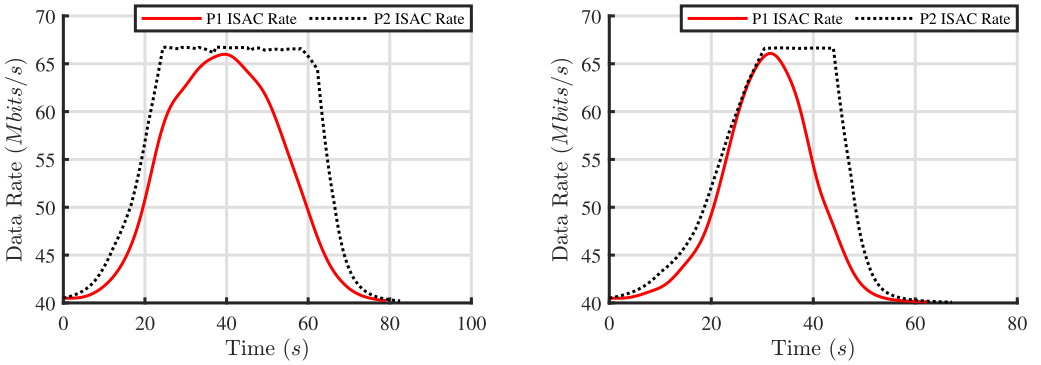

(c) $V_T = 10$m/s. (d) $V_T = 15$m/s.

Fig. 9. Real time ISAC data rate.

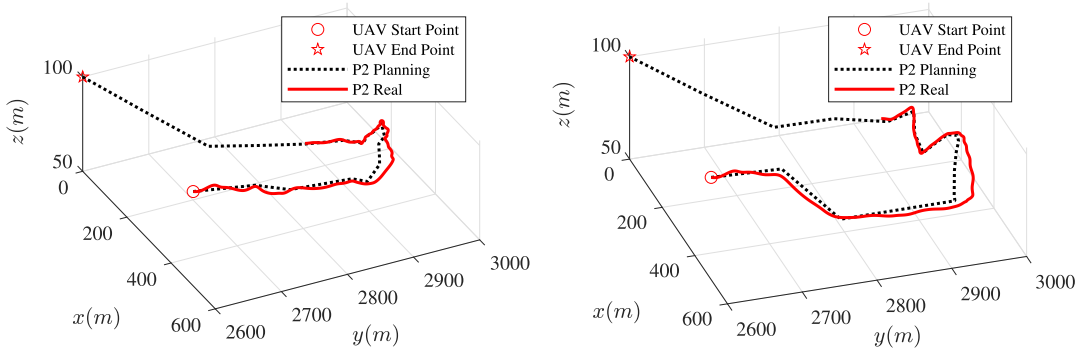

(a) Static target. (b) Moving target with a speed of 5 m/s.

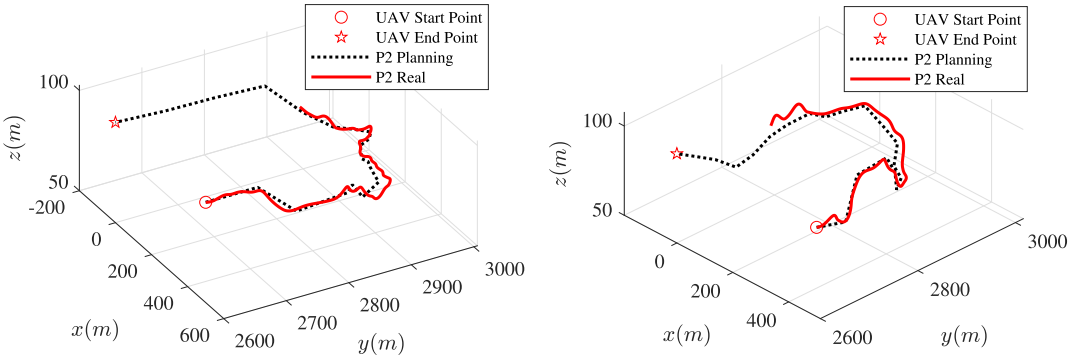

(c) Moving target with a speed of 10 m/s. (d) Moving target with a speed of 15 m/s.

Fig. 10. The planned P2 trajectory and its real trajectory.

Therefore, the real performance of P2 is less than that of P1, as illustrated in Fig. 7.

VI. Conclusion and Future Work

This manuscript considers a novel UAV-enabled ISAC system, where the UAV acts as an aerial platform equipped with full-duplex antennas and vision sensors to sense a single target of interest and transmits the sensing data in real time to a BS. A JDCSC scheme for UAV has been developed, which has been formulated as a dynamic optimization problem. The control parameterization method has been utilized to discretize infinite-dimensional decision variables and the exact penalty function has been adopted to deal with infinite-dimensional state constraints. The dynamic optimization problem is converted into a nonlinear problem. Simulation results show that the UAV-ISAC system can significantly improve the perceptual performance compared with the BS-ISAC system. Moreover, the proposed method outperforms the existing design which only considers the kinematics of the UAV.

The study can be extended to scenarios involving multiple UAVs, multiple targets, and operations across cellular networks. For example, when multiple UAVs work together to detect multiple targets, it presents challenges in task allocation and resource management that are crucial for improving accuracy. Furthermore, optimizing the flight trajectories of multiple UAVs to mitigate inter-cell interference and reduce disruptions among them is essential for enhancing the overall communication and sensing performance of the system.

Appendix A
Proof of Theorem 1

Since the UAV-ISAC system investigated in this manuscript operates causally, let's assume the UAV's feasible position $\boldsymbol{p}(t) \in \mathbb{P}$ and sensing power $P_r(t) \in \mathbb{P}_r$. In this context, the feasible solution for the communication power can be expressed as follows:

$$\begin{aligned} P_c(t) &\geq f_p\left(\boldsymbol{q}(t), P_r(t), \boldsymbol{x}_T(t)\right) \\ &\triangleq \left[\left(1+\mathrm{SINR_r}\right)^{\frac{\rho}{1-\rho}} 2^{r_v}-1\right] \frac{\|\boldsymbol{q}(t)-\boldsymbol{x}_B(t)\|^2}{\lambda_c}, \\ 0 &\leq P_c(t) \leq P_{max},\ C_6, \end{aligned}$$

where $\mathrm{SINR_r} = \frac{\lambda_r P_r(t)}{\|\boldsymbol{q}(t)-\boldsymbol{x}_T(t)\|^4}$ and $r_v = R_v/\left(B(1-\rho)\right)$. Given that R_v is a constant significantly greater than 0, it is straightforward to observe that $\inf_{\boldsymbol{p}(t)\in\mathbb{P}, P_r(t)\in\mathbb{P}_r}\left(\boldsymbol{q}(t), P_r(t), \boldsymbol{x}_T(t)\right) > 0$. Consequently, when $P_c(t)$ reaches its lower bound, the UAV achieves the minimum communication power consumption while satisfying the energy constraint C_6. Considering the feasible domain of $P_c(t)$, we can express the optimal $P_c^*(t)$ as:

$$P_c^*(t) = f_p\left(\boldsymbol{q}^*(t), P_r^*(t), \boldsymbol{x}_T(t)\right), \tag{40}$$

subject to $f_p\left(\boldsymbol{q}^*(t), P_r^*(t), \boldsymbol{x}_T(t)\right) \leq P_{max}$.

Appendix B
Proof of Theorem 2

We define a general problem, in which we need to find a system parameter vector $\boldsymbol{\sigma}$ such that the cost function

$$\mathcal{J}(\boldsymbol{\sigma}) = \Psi\left(\boldsymbol{x}(\tau_0|\boldsymbol{\sigma}), \boldsymbol{\sigma}\right) + \int_0^{\tau_0} \mathcal{L}\left(t, \boldsymbol{x}(t|\boldsymbol{\sigma}), \boldsymbol{\sigma}\right) \mathrm{d}t \tag{41}$$

is minimized subject to the dynamic system

$$\dot{\boldsymbol{x}}(t) = \boldsymbol{f}\left(t, \boldsymbol{x}(t), \boldsymbol{\sigma}, P_c(s)\right), \tag{42}$$

with initial conditions $\boldsymbol{x}(0) = \boldsymbol{x}_0(\boldsymbol{\sigma})$. The gradients of the cost function $\mathcal{J}$ are given in Lemma 1.

Lemma 1 (Theorem 7.2.2 in [53]): The gradients of the cost function $\mathcal{J}$ are given by

$$\begin{aligned} \frac{\partial \mathcal{J}(\boldsymbol{\sigma})}{\partial \boldsymbol{\sigma}} &= \frac{\partial \Psi\left(\boldsymbol{x}(T|\boldsymbol{\sigma}), \boldsymbol{\sigma}\right)}{\partial \boldsymbol{\sigma}} + \boldsymbol{\lambda}_0^T(0|\boldsymbol{\sigma}) \frac{\partial \boldsymbol{x}_0(\boldsymbol{\sigma})}{\partial \boldsymbol{\sigma}} \\ &\quad + \int_0^{\tau_0} \frac{\partial \mathcal{H}\left(t, \boldsymbol{x}(t|\boldsymbol{\sigma}), \boldsymbol{\sigma}, \boldsymbol{\lambda}(t|\boldsymbol{\sigma})\right)}{\partial \boldsymbol{\sigma}} \mathrm{d}t, \end{aligned}$$

where

$$\mathcal{H}\left(t, \boldsymbol{x}(t|\boldsymbol{\sigma}), \boldsymbol{\sigma}, \boldsymbol{\lambda}(t|\boldsymbol{\sigma})\right) = \mathcal{L}(t, \boldsymbol{x}(t), \boldsymbol{\sigma}) + \boldsymbol{\lambda}(t)^\top \boldsymbol{f}(\boldsymbol{x}(t), \boldsymbol{\sigma})$$

is the Hamiltonian and $\boldsymbol{\lambda}(t)$ is the co-state vector satisfying the following equations:

$$\left(\dot{\boldsymbol{\lambda}}(t)\right)^\top = -\frac{\partial \mathcal{H}\left(t, \boldsymbol{x}(t|\boldsymbol{\sigma}), \boldsymbol{\sigma}, \boldsymbol{\lambda}(t|\boldsymbol{\sigma})\right)}{\partial \boldsymbol{x}}$$

with

$$\left(\boldsymbol{\lambda}(\tau_0)\right)^\top = \frac{\partial \Psi\left(\boldsymbol{x}(\tau_0|\boldsymbol{\sigma})\right)}{\partial \boldsymbol{x}}.$$

According to Lemma 1, we define the Hamiltonian function of the $(\mathbf{P1})_{\sigma,\epsilon}$ as

$$H = \Delta_i + T\boldsymbol{\lambda}(s)^\top \boldsymbol{f}\left(\boldsymbol{x}(s), \boldsymbol{\sigma}, P_c(s)\right) \tag{43}$$

and $\boldsymbol{\lambda}(s)$ is the corresponding co-state vector satisfying the following differential equations

$$\dot{\boldsymbol{\lambda}}(s) = -\frac{\partial H}{\partial \boldsymbol{x}}^\top \tag{44}$$

with

$$\boldsymbol{\lambda}(1) = \frac{\partial\left(-x_{16}(1) + \Delta_e + \Delta_{ine}\right)}{\partial \boldsymbol{x}}^\top. \tag{45}$$

The objective function J is defined as

$$J = \Psi_0 + \int_0^1 \Delta_i \mathrm{d}s, \tag{46}$$

where $\Psi_0 = -Q_r(1) + \delta\epsilon^\gamma + \Delta_e + \Delta_{ine}$. We can obtain the following gradient formulas:

$$\begin{aligned} &\frac{\partial \Psi_0}{\partial \boldsymbol{\sigma}} = 0,\ \frac{\partial \Psi_0}{\partial T} = 0,\ \frac{\partial \Psi_0}{\partial \epsilon} \\ &\quad = \delta\gamma\epsilon^{\gamma-1} - \alpha\epsilon^{-\alpha-1}\left(\Delta_e + \Delta_{ine}\right). \end{aligned} \tag{47}$$

Because $\boldsymbol{x}_0$ does not depend on $\boldsymbol{\sigma}$, T and ϵ, we have

$$\frac{\partial \boldsymbol{x}_0}{\partial \boldsymbol{u}} = 0,\ \frac{\partial \boldsymbol{x}_0}{\partial T} = 0,\ \frac{\partial \boldsymbol{x}_0}{\partial \epsilon} = 0. \tag{48}$$

Therefore, the gradients of the objective functional J with respect to $\boldsymbol{\sigma}$, T and ϵ are

$$\begin{aligned}
\frac{\partial J}{\partial \boldsymbol{\sigma}} &= \int_0^1 \frac{\partial H}{\partial \boldsymbol{\sigma}} \mathrm{d}s, \\
\frac{\partial J}{\partial T} &= \int_0^1 \frac{\partial H}{\partial T} \mathrm{d}s, \\
\frac{\partial J}{\partial \epsilon} &= \frac{\partial \Psi_0}{\partial \epsilon} + \int_0^1 \frac{\partial H}{\partial \epsilon} \mathrm{d}s \\
&= \delta\gamma\epsilon^{\gamma-1} - \alpha\epsilon^{-\alpha-1}\left(\Delta_e + \Delta_{ine} + T\int_0^1 \Delta_i \mathrm{d}s\right) \\
&\quad + 2\beta\epsilon^{\beta-\alpha-1} T \int_0^1 \left[W_1 \min\left\{0,\ x_3(s) - h_{min} + \epsilon^\beta W_1\right\}\right. \\
&\quad + W_1 \min\left\{0,\ h_{max} - x_3(s) + \epsilon^\beta W_1\right\} \\
&\quad \left. + W_2 \min\left\{0,\ P_{max} - f_p(s) + \epsilon^\beta W_2\right\}\right] \mathrm{d}s,
\end{aligned}$$

where $f_p(s) = f_p\left(\boldsymbol{q}(s), \sigma_{5,k}, \boldsymbol{x}_T(s)\right)$. So far, the proof of Theorem 2 is completed.

REFERENCES

[1] ITU-R. (2023). *M.2160: Framework and Overall Objectives of the Future Development of IMT for 2030 and Beyond*. [Online]. Available: https://www.itu.int/rec/R-REC-M.2160/en

[2] W. Yuan, F. Liu, C. Masouros, J. Yuan, D. W. K. Ng, and N. González-Prelcic, "Bayesian predictive beamforming for vehicular networks: A low-overhead joint radar-communication approach," *IEEE Trans. Wireless Commun.*, vol. 20, no. 3, pp. 1442–1456, Mar. 2021.

[3] X. Liu, T. Huang, N. Shlezinger, Y. Liu, J. Zhou, and Y. C. Eldar, "Joint transmit beamforming for multiuser MIMO communications and MIMO radar," *IEEE Trans. Signal Process.*, vol. 68, pp. 3929–3944, 2020.

[4] C. Xu, B. Clerckx, S. Chen, Y. Mao, and J. Zhang, "Rate-splitting multiple access for multi-antenna joint radar and communications," *IEEE J. Sel. Topics Signal Process.*, vol. 15, no. 6, pp. 1332–1347, Nov. 2021.

[5] J. A. Zhang et al., "Enabling joint communication and radar sensing in mobile networks—A survey," *IEEE Commun. Surveys Tuts.*, vol. 24, no. 1, pp. 306–345, 1st Quart., 2022.

[6] F. Liu, C. Masouros, A. P. Petropulu, H. Griffiths, and L. Hanzo, "Joint radar and communication design: Applications, state-of-the-art, and the road ahead," *IEEE Trans. Commun.*, vol. 68, no. 6, pp. 3834–3862, Jun. 2020.

[7] Q. Wu et al., "A comprehensive overview on 5G-and-beyond networks with UAVs: From communications to sensing and intelligence," *IEEE J. Sel. Areas Commun.*, vol. 39, no. 10, pp. 2912–2945, Oct. 2021.

[8] W. Mei and R. Zhang, "Uplink cooperative NOMA for cellular-connected UAV," *IEEE J. Sel. Topics Signal Process.*, vol. 13, no. 3, pp. 644–656, Jun. 2019.

[9] W. Mei and R. Zhang, "Cooperative downlink interference transmission and cancellation for cellular-connected UAV: A divide-and-conquer approach," *IEEE Trans. Commun.*, vol. 68, no. 2, pp. 1297–1311, Feb. 2020.

[10] W. Mei and R. Zhang, "Aerial-ground interference mitigation for cellular-connected UAV," *IEEE Wireless Commun.*, vol. 28, no. 1, pp. 167–173, Feb. 2021.

[11] C. Zhan and Y. Zeng, "Energy minimization for cellular-connected UAV: From optimization to deep reinforcement learning," *IEEE Trans. Wireless Commun.*, vol. 21, no. 7, pp. 5541–5555, Jul. 2022.

[12] J. Mu, R. Zhang, Y. Cui, N. Gao, and X. Jing, "UAV meets integrated sensing and communication: Challenges and future directions," *IEEE Commun. Mag.*, vol. 61, no. 5, pp. 62–67, May 2023.

[13] K. Meng et al., "Throughput maximization for UAV-enabled integrated periodic sensing and communication," *IEEE Trans. Wireless Commun.*, vol. 22, no. 1, pp. 671–687, Jan. 2023.

[14] K. Meng, D. Li, X. He, and M. Liu, "Space pruning based time minimization in delay constrained multi-task UAV-based sensing," *IEEE Trans. Veh. Technol.*, vol. 70, no. 3, pp. 2836–2849, Mar. 2021.

[15] Z. Lyu, G. Zhu, and J. Xu, "Joint maneuver and beamforming design for UAV-enabled integrated sensing and communication," *IEEE Trans. Wireless Commun.*, vol. 22, no. 4, pp. 2424–2440, Apr. 2023.

[16] R. Mahony, V. Kumar, and P. Corke, "Multirotor aerial vehicles: Modeling, estimation, and control of quadrotor," *IEEE Robot. Autom. Mag.*, vol. 19, no. 3, pp. 20–32, Sep. 2012.

[17] B. Li, Q. Li, Y. Zeng, Y. Rong, and R. Zhang, "3D trajectory optimization for energy-efficient UAV communication: A control design perspective," *IEEE Trans. Wireless Commun.*, vol. 21, no. 6, pp. 4579–4593, Jun. 2022.

[18] B. Li, J. Zhang, L. Dai, K. L. Teo, and S. Wang, "A hybrid offline optimization method for reconfiguration of multi-UAV formations," *IEEE Trans. Aerosp. Electron. Syst.*, vol. 57, no. 1, pp. 506–520, Feb. 2021.

[19] G. Liu, B. Li, and Y. Ji, "A modified HP-adaptive pseudospectral method for multi-UAV formation reconfiguration," *ISA Trans.*, vol. 129, pp. 217–229, Oct. 2022.

[20] S. Shao, C. He, Y. Zhao, and X. Wu, "Efficient trajectory planning for UAVs using hierarchical optimization," *IEEE Access*, vol. 9, pp. 60668–60681, 2021.

[21] H. Sandhu, P. P. Pradhan, K. Rajawat, and M. Kothari, "Minimum time trajectory optimization for a 6-DoF quadrotor UAV using successive convexification," in *Proc. AIAA SCITECH Forum*, Orlando, FL, USA, Jan. 2024, p. 92.

[22] Z. Shen, G. Zhou, H. Huang, C. Huang, Y. Wang, and F.-Y. Wang, "Convex optimization-based trajectory planning for quadrotors landing on aerial vehicle carriers," *IEEE Trans. Intell. Vehicles*, vol. 9, no. 1, pp. 138–150, Jan. 2024.

[23] Y. Liu, H. Wang, J. Fan, J. Wu, and T. Wu, "Control-oriented UAV highly feasible trajectory planning: A deep learning method," *Aerosp. Sci. Technol.*, vol. 110, Mar. 2021, Art. no. 106435.

[24] Y. Wang, H. Wang, Y. Liu, J. Wu, and Y. Lun, "6-DOF UAV path planning and tracking control for obstacle avoidance: A deep learning-based integrated approach," *Aerosp. Sci. Technol.*, vol. 151, Aug. 2024, Art. no. 109320.

[25] Z. Xiao and Y. Zeng, "Waveform design and performance analysis for full-duplex integrated sensing and communication," *IEEE J. Sel. Areas Commun.*, vol. 40, no. 6, pp. 1823–1837, Jun. 2022.

[26] F. T. Faul, D. Korthauer, and T. F. Eibert, "Impact of rotor blade rotation of UAVs on electromagnetic field measurements," *IEEE Trans. Instrum. Meas.*, vol. 70, pp. 1–9, 2021.

[27] Z. Ma et al., "Impact of UAV rotation on MIMO channel characterization for air-to-ground communication systems," *IEEE Trans. Veh. Technol.*, vol. 69, no. 11, pp. 12418–12431, Nov. 2020.

[28] J. Bao et al., "Impact of 6D mobility on Doppler characteristics of UAV-to-vehicle channels," in *Proc. 18th Eur. Conf. Antennas Propag. (EuCAP)*, Glasgow, U.K., Mar. 2024, pp. 1–5.

[29] E. S. Kang, H. Hwang, and D. S. Han, "A fine carrier recovery algorithm robustto Doppler shift for OFDM systems," *IEEE Trans. Consum. Electron.*, vol. 56, no. 3, pp. 1218–1222, Aug. 2010.

[30] Q. Wu, L. Liu, and R. Zhang, "Fundamental trade-offs in communication and trajectory design for UAV-enabled wireless network," *IEEE Wireless Commun.*, vol. 26, no. 1, pp. 36–44, Feb. 2019.

[31] M. Xing, X. Jiang, R. Wu, F. Zhou, and Z. Bao, "Motion compensation for UAV SAR based on raw radar data," *IEEE Trans. Geosci. Remote Sens.*, vol. 47, no. 8, pp. 2870–2883, Aug. 2009.

[32] M. Pieraccini, L. Miccinesi, and N. Rojhani, "A Doppler range compensation for step-frequency continuous-wave radar for detecting small UAV," *Sensors*, vol. 19, no. 6, p. 1331, Mar. 2019.

[33] L. Zhang, J. Yang, Z. Zhang, and P. Cai, "A cooperative localization algorithm based on UAV platform," in *Proc. Int. Conf. Adv. Comput. Endogenous Secur.*, Nanjing, China, Apr. 2022, pp. 1–5.

[34] M. Li, J. Lang, and M. Liu, "Ground targets passive location by multiple UAVs," in *Proc. IEEE 23rd Int. Conf. Commun. Technol. (ICCT)*, Wuxi, China, Oct. 2023, pp. 272–275.

[35] J. Wu, W. Yuan, F. Liu, Y. Cui, X. Meng, and H. Huang, "UAV-based target tracking: Integrating sensing into communication signals," in *Proc. IEEE/CIC Int. Conf. Commun. China (ICCC Workshops)*, Foshan, China, Aug. 2022, pp. 309–313.

[36] D. W. Bliss, "Cooperative radar and communications signaling: The estimation and information theory odd couple," in *Proc. IEEE Radar Conf.*, Cincinnati, OH, USA, May 2014, pp. 50–55.

[37] B. Paul and D. W. Bliss, "Extending joint radar-communications bounds for FMCW radar with Doppler estimation," in *Proc. IEEE Radar Conf. (RadarCon)*, May 2015, pp. 89–94.

[38] A. R. Chiriyath, B. Paul, G. M. Jacyna, and D. W. Bliss, "Inner bounds on performance of radar and communications co-existence," *IEEE Trans. Signal Process.*, vol. 64, no. 2, pp. 464–474, Jan. 2016.

[39] A. R. Chiriyath, B. Paul, and D. W. Bliss, "Radar-communications convergence: Coexistence, cooperation, and co-design," *IEEE Trans. Cognit. Commun. Netw.*, vol. 3, no. 1, pp. 1–12, Mar. 2017.
[40] T. T. Nguyen, K. Elbassioni, N. C. Luong, D. Niyato, and D. I. Kim, "Access management in joint sensing and communication systems: Efficiency versus fairness," *IEEE Trans. Veh. Technol.*, vol. 71, no. 5, pp. 5128–5142, May 2022.
[41] Q. Zhang, X. Wang, Z. Li, and Z. Wei, "Design and performance evaluation of joint sensing and communication integrated system for 5G mmWave enabled CAVs," *IEEE J. Sel. Topics Signal Process.*, vol. 15, no. 6, pp. 1500–1514, Nov. 2021.
[42] M. Thomas and A. T. Joy, *Elements of Information Theory*. Hoboken, NJ, USA: Wiley, 2006.
[43] Q. Zhang, H. Sun, X. Gao, X. Wang, and Z. Feng, "Time-division ISAC enabled connected automated vehicles cooperation algorithm design and performance evaluation," *IEEE J. Sel. Areas Commun.*, vol. 40, no. 7, pp. 2206–2218, Jul. 2022.
[44] M. A. Richards, J. Scheer, W. A. Holm, and W. L. Melvin, *Principles of Modern Radar*. Princeton, NJ, USA: Citeseer, 2010.
[45] T. N. Le Long and H. N. Nguyen, "Research on data transmission rate of optical camera communication using LEDs for positioning system in buildings," in *Proc. Int. Conf. Adv. Technol. Commun. (ATC)*, Ha Noi, Vietnam, Oct. 2022, pp. 80–85.
[46] S.-H. Park, O. Simeone, O. Sahin, and S. Shamai (Shitz), "Joint precoding and multivariate backhaul compression for the downlink of cloud radio access networks," *IEEE Trans. Signal Process.*, vol. 61, no. 22, pp. 5646–5658, Nov. 2013.
[47] D. Wen et al., "Task-oriented sensing, computation, and communication integration for multi-device edge AI," in *Proc. IEEE Int. Conf. Commun.*, Rome, Italy, May 2023, pp. 3608–3613.
[48] H. Liu, X. Wang, and Y. Zhong, "Quaternion-based robust attitude control for uncertain robotic quadrotors," *IEEE Trans. Ind. Informat.*, vol. 11, no. 2, pp. 406–415, Apr. 2015.
[49] J. T.-Y. Wen and K. Kreutz-Delgado, "The attitude control problem," *IEEE Trans. Autom. Control*, vol. 36, no. 10, pp. 1148–1162, Oct. 1991.
[50] J. C. K. Chou, "Quaternion kinematic and dynamic differential equations," *IEEE Trans. Robot. Autom.*, vol. 8, no. 1, pp. 53–64, Feb. 1992.
[51] Z. Bubnicki, *Modern Control Theory*. Cham, Switzerland: Springer, 2005.
[52] B. Li, C. Xu, K. L. Teo, and J. Chu, "Time optimal Zermelo's navigation problem with moving and fixed obstacles," *App. Math. Com.*, vol. 224, pp. 866–875, Nov. 2013.
[53] K. L. Teo, B. Li, C. Yu, and V. Rehbock, *Applied and Computational Optimal Control: A Control Parametrization Approach*. Cham, Switzerland: Springer, 2021.
[54] B. Li, C. J. Yu, K. L. Teo, and G. R. Duan, "An exact penalty function method for continuous inequality constrained optimal control problem," *J. Optim. Theory Appl.*, vol. 151, no. 2, pp. 260–291, Sep. 2011.
[55] P. T. Boggs and J. W. Tolle, "Sequential quadratic programming," *Acta Numer.*, vol. 4, pp. 1–51, Jan. 1995.
[56] P. E. Gill, W. Murray, and M. A. Saunders, "SNOPT: An SQP algorithm for large-scale constrained optimization," *SIAM Rev.*, vol. 47, no. 1, pp. 99–131, Jan. 2005.

Qingliang Li (Graduate Student Member, IEEE) received the B.E. degree in flight vehicle control and information engineering and the M.E. degree in electronic information from Sichuan University, China, in 2020 and 2023, respectively. He is currently pursuing the Ph.D. degree with the National Key Laboratory of Wireless Communications, University of Electronic Science and Technology of China (UESTC), China. His research interests include sensing, communication and control co-design, and deep reinforcement learning.

Bin Li (Senior Member, IEEE) received the bachelor's degree in automation and the master's and Ph.D. degrees in control science and engineering from Harbin Institute of Technology, China, in 2005, 2008, and 2011, respectively. From 2012 to 2014, he was a Research Associate with the School of Electrical, Electronic and Computer Engineering, The University of Western Australia, Australia. From 2014 to 2017, he was a Research Fellow with the Department of Mathematics and Statistics, Curtin University, Australia. Since 2017, he has been a Professor with Sichuan University, China. His research interests include model predictive control, optimal control, optimization, signal processing, and wireless communications.

Zhen-Qing He (Member, IEEE) received the Ph.D. degree in communication and information systems from the University of Electronic Science and Technology of China (UESTC), Chengdu, China, in 2017. He was a Post-Doctoral Researcher and an Associate Research Fellow with the National Key Laboratory of Science and Technology on Communications, UESTC, from 2018 to 2020 and from 2021 to 2022, respectively. He is currently an Associate Professor with the School of Aeronautics and Astronautics, Sichuan University, Chengdu. His main research interests include a broad range of signal processing, wireless communications, and machine learning.

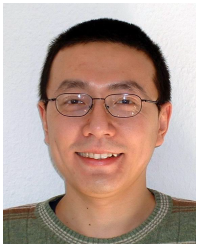

Yue Rong (Senior Member, IEEE) received the Ph.D. degree (summa cum laude) in electrical engineering from Darmstadt University of Technology, Darmstadt, Germany, in 2005. He was a Post-Doctoral Researcher with the Department of Electrical Engineering, University of California at Riverside, Riverside, CA, USA, from February 2006 to November 2007. Since December 2007, he has been with Curtin University, Bentley, WA, Australia, where he is currently a Professor. His research interests include signal processing for communications, underwater acoustic communications, underwater optical wireless communications, machine learning, speech recognition, and biomedical engineering. He has published over 200 journals and conference papers in these areas.

Zhu Han (Fellow, IEEE) received the B.S. degree in electronic engineering from Tsinghua University, Beijing, China, in 1997, and the M.S. and Ph.D. degrees in electrical and computer engineering from the University of Maryland, College Park, in 1999 and 2003, respectively. From 2000 to 2002, he was a Research and Development Engineer with JDSU, Germantown, MD, USA. From 2003 to 2006, he was a Research Associate with the University of Maryland. From 2006 to 2008, he was an Assistant Professor with Boise State University, Boise, ID, USA. Currently, he is a John and Rebecca Moores Professor with the Electrical and Computer Engineering Department and the Computer Science Department, University of Houston, Houston, TX, USA. His main research interests include the novel game-theory-related concepts critical to enabling efficient and distributive use of wireless networks with limited resources, wireless resource allocation and management, wireless communications and networking, quantum computing, data science, smart grids, carbon neutralization, and security and privacy.